Supplemental Information

A Bioinformatics 3D Cellular Morphotyping Strategy for Assessing Biomaterial Scaffold Niches

Stephen J. Florczyk, Mylene Simon, Derek Juba, P. Scott Pine, Sumona Sarkar, Desu Chen, Paula J. Baker, Subhadip Bodhak, Antonio Cardone, Mary C. Brady, Peter Bajcsy, and Carl G. Simon, Jr.

Number of pages in Supplemental Information: 23

Number of supplemental figures: 9

Supplemental Methods

Shape metric verification

The algorithms used to calculate shape metrics were verified using a synthetic in silico Z-stack of a 3D sphere whose voxel dimensions matched that used for the confocal imaging of the cells (voxel dimensions of X = 0.240 µm; Y = 0.240 µm, Z = 0.713 µm; sphere dimensions of X-axis dia. = 15.12 µm, Y-axis dia. = 15.12 µm, Z-axis dia. = 14.97 µm). The metric values computed for the in silico sphere were compared with ideal values computed manually for a sphere with diameter 15 µm using mathematical formulae. While most metrics were verified to be accurate, projected perimeter and the surface area were complicated by the anisotropic voxel dimensions and required implementation of a modified algorithm.[1] The errors for shape metrics tested on in silico spheres was less than 2.0 % (Supplemental Fig. 9). The results demonstrated that the algorithms accurately quantified a shape with known dimensions and are suitable for analyzing cell shapes.

Assessment of performance of confocal imaging and image analysis pipeline

In order to assess the performance of the confocal imaging and image analysis pipeline, fluorescent microspheres with known diameter distributions were imaged and analyzed. A major source of confocal imaging error is distortion along the axial-axis (Z-axis) due to chromatic aberrations. The chromatic aberrations are caused by differences in refractive indices (RI) of the components of imaging train that prevent the light from converging at the desired focal point. Our imaging train consists of objective (RI = 1.33, as given by the manufacturer), Dulbecco's phosphate buffered saline (D-PBS) (RI = 1.33)[2] and cells (RI = 1.36 to 1.40).[3] In some cases, the substrate will provide an additional RI (MG, CG, FG). Chromatic aberrations are also dependent

on wavelength, with greater distortions at longer wavelengths. Chromatic aberrations can be assessed using microspheres of known diameter labelled with appropriate fluors.

Microspheres labeled with fluors corresponding to the two channels used for cell imaging were imaged: FluoSpheres polystyrene microspheres, blue (emission 365 nm, excitation 415 nm, cat. # F-8837), 14.6 ± 0.146 µm diameter, and orange (emission 540 nm, excitation 560 nm, cat. # F-8841), 14.8 ± 0.061 µm diameter (Life Technologies). Five microspheres were imaged in D-PBS for both the actin and nucleus channels using the same confocal microscope settings and voxel dimensions as were used for imaging cells. Microsphere Z-stacks were processed and segmented in the same manner as the cell Z-stacks and shape metrics were computed. Microsphere shape metrics determined from the confocal imaging pipeline were compared with ideal values computed manually for a microsphere with the diameter matching that of the appropriate microspheres (14.8 µm dia. for actin channel, 14.6 µm dia. for nucleus channel) using mathematical formulae.

The errors for the shape features are less than 35% and 55% for orange and blue beads, respectively (Supplemental Fig. 9). These errors arise from the influence of chromatic aberrations in the CLSM imaging and constraints imposed by voxel dimensions, which included greater XY resolution than Z resolution. The metrics most affected by the errors were those that incorporated Z-axis components or were not oriented to the gyration tensor ellipsoid. Despite these errors, L_1-depth had low error compared to the other shape metrics evaluated. Since the refractive index of the polystyrene spheres (RI = 1.59)[4] is different from cells (RI = 1.36 to 1.40), it is not possible to use the microsphere results to generate a deconvolution correction factor. A potential topic for future work would be to generate highly uniform microspheres with a refractive index that matches cells and which are labeled with fluors of interest. It may be possible to make fluorescently labeled, uniform diameter, crosslinked poly(ethylene glycol) bead with a RI that matches cells.[5] The RI-

matched microspheres could be added to substrates alongside cells and imaged in parallel to generate an accurate correction factor for chromatic aberrations. These errors are systemic to confocal microscopy and other fluorescent microscopy imaging. Such errors could be reduced with a smaller step size between Z-frames, ideally based on the Z-resolution limit, but this is a tradeoff between acquisition time and Z-resolution. While some of the relative errors reported are as high as 35% and 55%, all cells comprising the dataset have the same errors affecting the cell shape measurements indicating that relative comparisons within the data set are meaningful.

References

(1) Lindblad, J., Surface area estimation of digitized 3D objects using weighted local configurations. *Image and Vision Computing* **2005,** *23* (2), 111-122.

(2) Chaitavon, K.; Sumriddetchkajorn, S.; Nukeaw, J., Highly sensitive refractive index measurement with a sandwiched single-flow-channel micofluidic chip. *RSC Advances* **2013,** *3* (19), 6981-6984.

(3) Choi, W.; Fang-Yen, C.; Badizadegan, K.; Oh, S.; Lue, N.; Dasari, R. R.; Feld, M. S., Tomographic phase microscopy. *Nature Methods* **2007,** *4* (9), 717-719.

(4) Liang, X. J.; Liu, A. Q.; Lim, C. S.; Ayi, T. C.; Yap, P. H., Determining refractive index of single living cell using an integrated microchip. *Sensors and Actuators A* **2007,** *133* (2), 349-354.

(5) Choi, M.; Choi, J. W.; Kim, S.; Nizamoglu, S.; Hahn, S. K.; Yun, S. H., Light-guiding hydrogels for cell-based sensing and optogenetic synthesis in vivo. *Nature Photonics* **2013,** *7* (2), 987-994.

#	Shape Metric	Notes	Metrics Used in Dendrograms & PCA Analyses	
			Actin	Nucleus
1	L_3-Depth	Caliper length along L_3-axis	X	X
2	L_2-Depth	Caliper length along L_2-axis	X	X
3	L_1-Depth	Caliper length along L_1-axis	X	X
4	X-Depth	Caliper length along the X-axis		
5	Y-Depth	Caliper length along the Y-axis		
6	Z-Depth	Caliper length along the Z-axis		
7	$\sqrt{(L_1)}$	From gyration tensor	X	X
8	$\sqrt{(L_2)}$	From gyration tensor	X	X
9	$\sqrt{(L_3)}$	From gyration tensor	X	X
10	Z-Perimeter	Perimeter from max projection along Z-axis		
11	Y-Perimeter	Perimeter from max projection along Y-axis		
12	X-Perimeter	Perimeter from max projection along X-axis		
13	L_1-Perimeter	Perimeter from max projection along L_1-axis	X	X
14	L_2-Perimeter	Perimeter from max projection along L_2-axis	X	X
15	L_3-Perimeter	Perimeter from max projection along L_3-axis	X	X
16	Surface area	3D surface area	X	X
17	Z-Area	Area from max projection along Z-axis (same as spread area)		
18	Y-Area	Area from max projection along Y-axis		
19	X-Area	Area from max projection along X-axis		
20	L_1-Area	Area from max projection along L_1-axis	X	X
21	L_2-Area	Area from max projection along L_2-axis	X	X
22	L_3-Area	Area from max projection along L_3-axis	X	X
23	Volume	Volume	X	X
24	Z-Aspect Ratio	Aspect ratio of bounding box for max projection along Z-axis		
25	Y-Aspect Ratio	Aspect ratio of bounding box for max projection along Y-axis		
26	X-Aspect Ratio	Aspect ratio of bounding box for max projection along X-axis		
27	L_1-Aspect Ratio	Aspect ratio of bounding box for max projection along L_1-axis	X	X
28	L_2-Aspect Ratio	Aspect ratio of bounding box for max projection along L_2-axis	X	X
29	L_3-Aspect Ratio	Aspect ratio of bounding box for max projection along L_3-axis	X	X
30	$\sqrt{(L_1/L_3)}$	Ratio of shortest gyration moment to longest gyration moment		
31	$\sqrt{(L_2/L_3)}$	Ratio of middle gyration moment to longest gyration moment		
32	$\sqrt{(L_1/L_2)}$	Ratio of shortest gyration moment to middle gyration moment		
33	$\sqrt{(L_3/L_1)}$	Ratio of longest gyration moment to shortest gyration moment	X	X
34	$\sqrt{(L_3/L_2)}$	Ratio of longest gyration moment to middle gyration moment	X	X
35	$\sqrt{(L_2/L_1)}$	Ratio of middle gyration moment to shortest gyration moment	X	X
36	Square radius of gyration	$Rg^2 = L_1 + L_2 + L_3$	X	X
37	Asphericity	$b = L_3 - 0.5(L_1 + L_2)$	X	X
38	Acylindricity	$c = L_2 - L_1$	X	X
39	Anisotropy	$\kappa^2 = (b^2 + (3/4)c^2) / Rg^4$	X	X
40	Nucleus to Actin Surface Area	Ratio of nucleus to actin surface area	X	
41	Nucleus to Actin Volume	Ratio of nucleus to actin volume	X	
42	Nucleus to Actin Distance	Distance from center-of-mass of nucleus to center-of-mass of actin using Euclidian distance	X	
43	Nucleus to Actin L_1-depth ratio	Ratio of nucleus L_1-depth to actin L_1-depth	X	

Fig. S1. Shape metrics calculated for the dataset. Metrics 1 – 39 apply for both actin and nucleus, while metrics 40 – 43 are ratios of nucleus to actin. Metrics denoted with X, Y, Z are obtained from the image stack without orientation. Metrics denoted with L_1, L_2, L_3 are obtained from the cells that have been oriented to their gyration tensor moments. In the two columns to the right, the metrics used for dendrogram and PCA analyses are denoted. A number of metrics were omitted from the dendrogram and PCA analyses since they were redundant with other metrics. For example, Z-area is a metric that comes from 2D imaging and it does not make sense to include it in the dendrogram and PCA analyses since the goal was to use 3D data.
More detailed information on the metric formulae can be found at this link: https://isg.nist.gov/deepzoomweb/measurement3Ddata_help#shape-metrics-formulas.

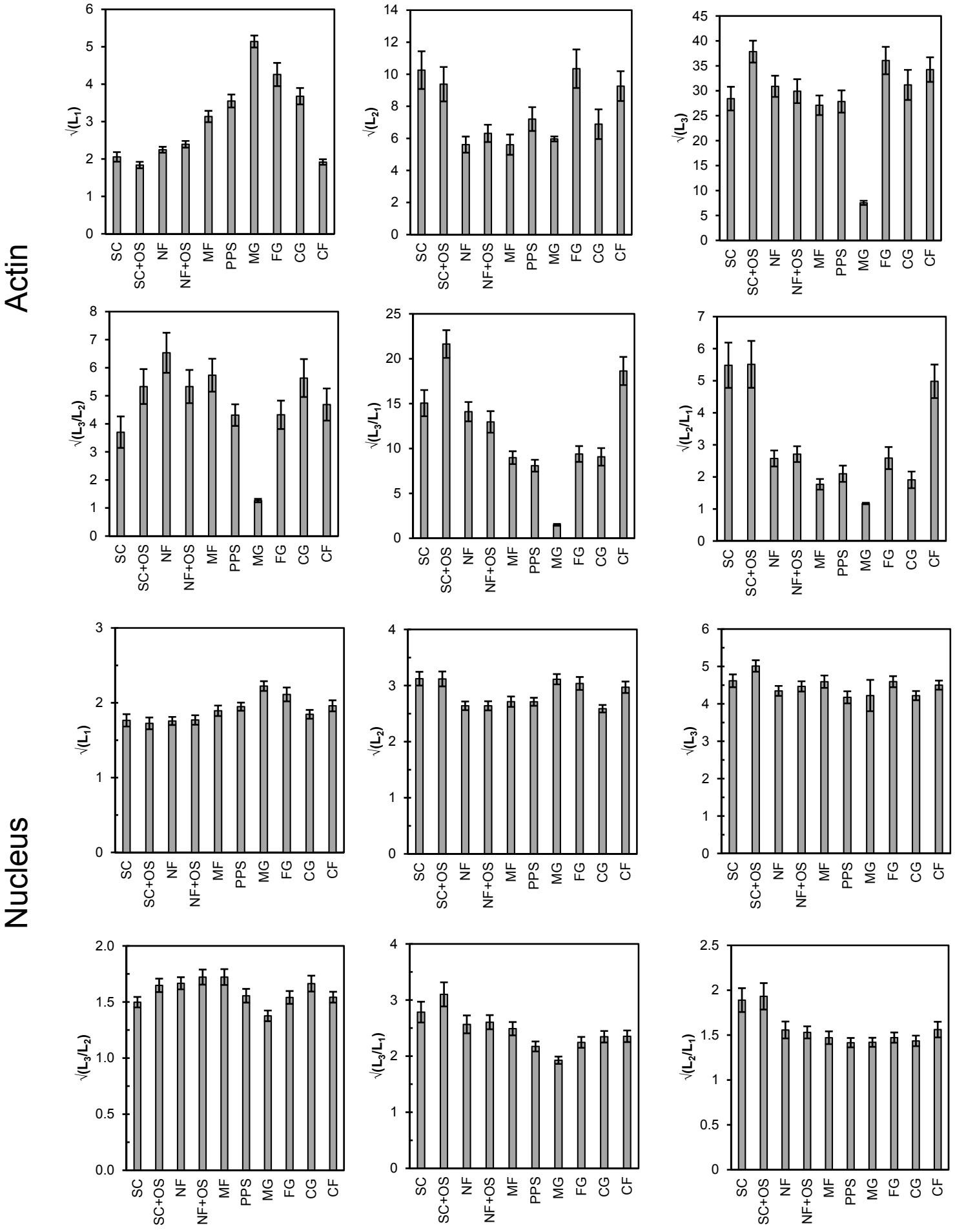

Fig. S2a. Shape metric plots. Approximately 100 cells were imaged for each scaffold (see Table 1) and error bars represent 2 standard deviations of the mean. Statistical analysis is in Fig. S3.

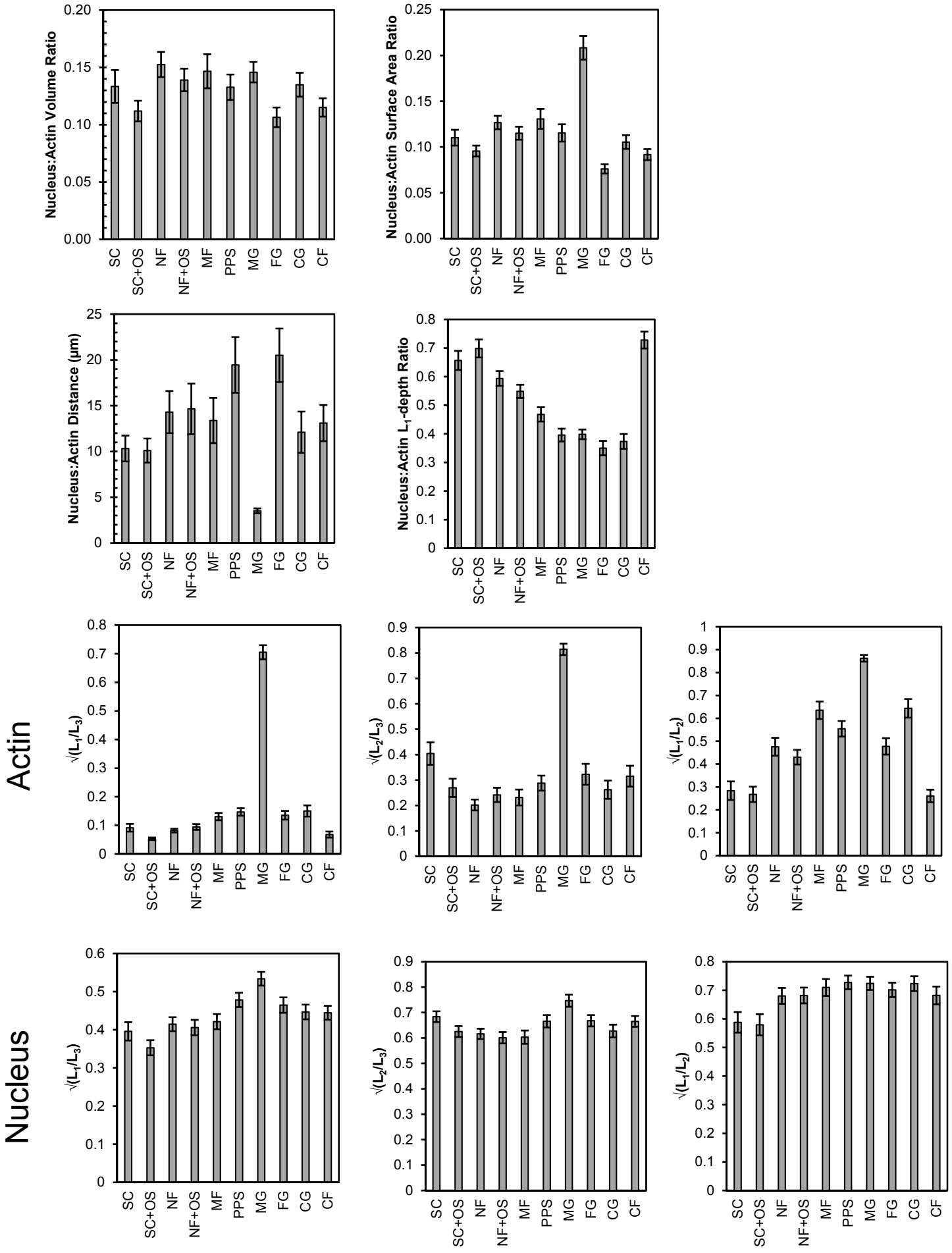

Fig. S2b. Shape metric plots. Approximately 100 cells were imaged for each scaffold (see Table 1) and error bars represent 2 standard deviations of the mean. Statistical analysis is in Fig. S3.

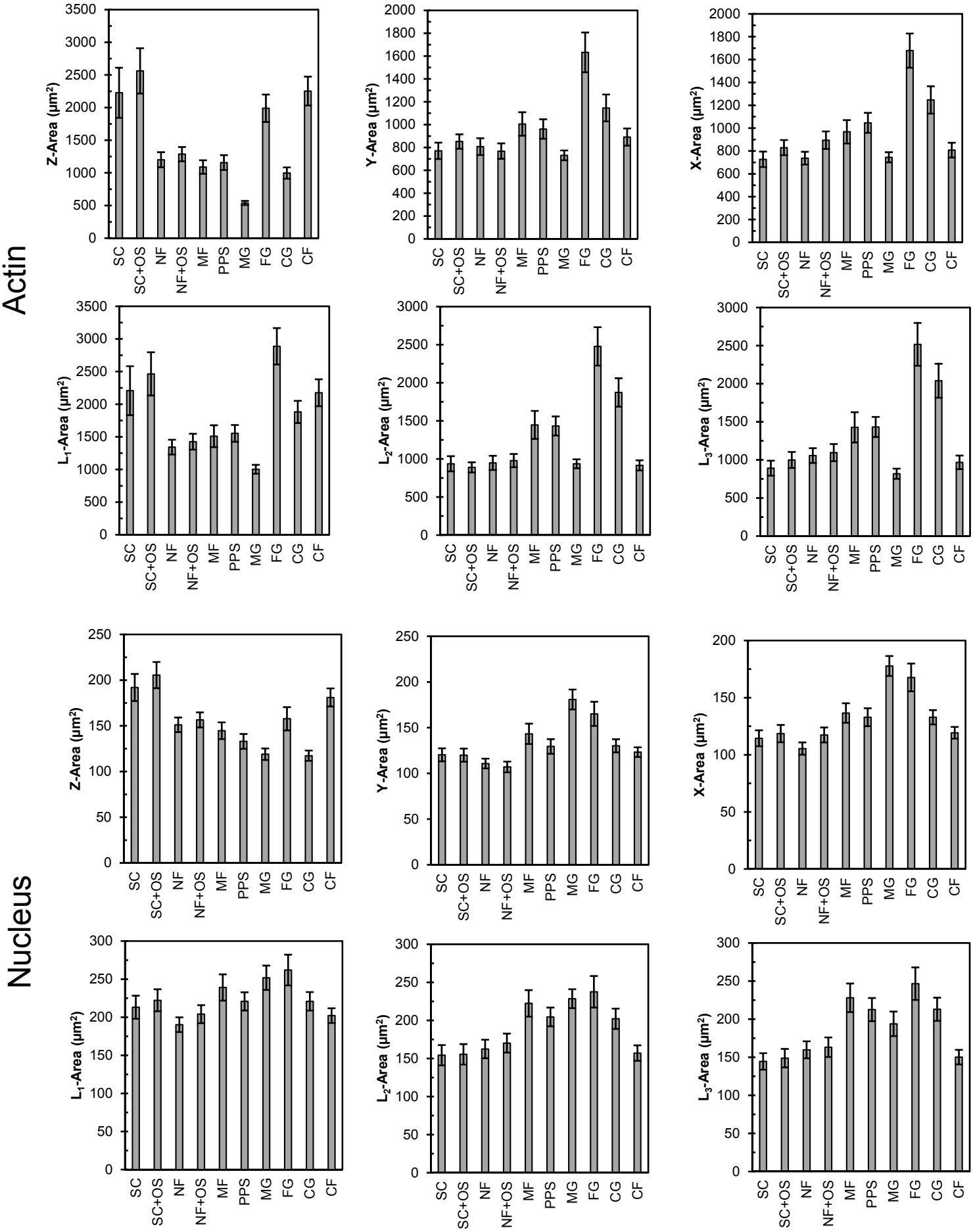

Fig. S2c. Shape metric plots. Approximately 100 cells were imaged for each scaffold (see Table 1) and error bars represent 2 standard deviations of the mean. Statistical analysis is in Fig. S3.

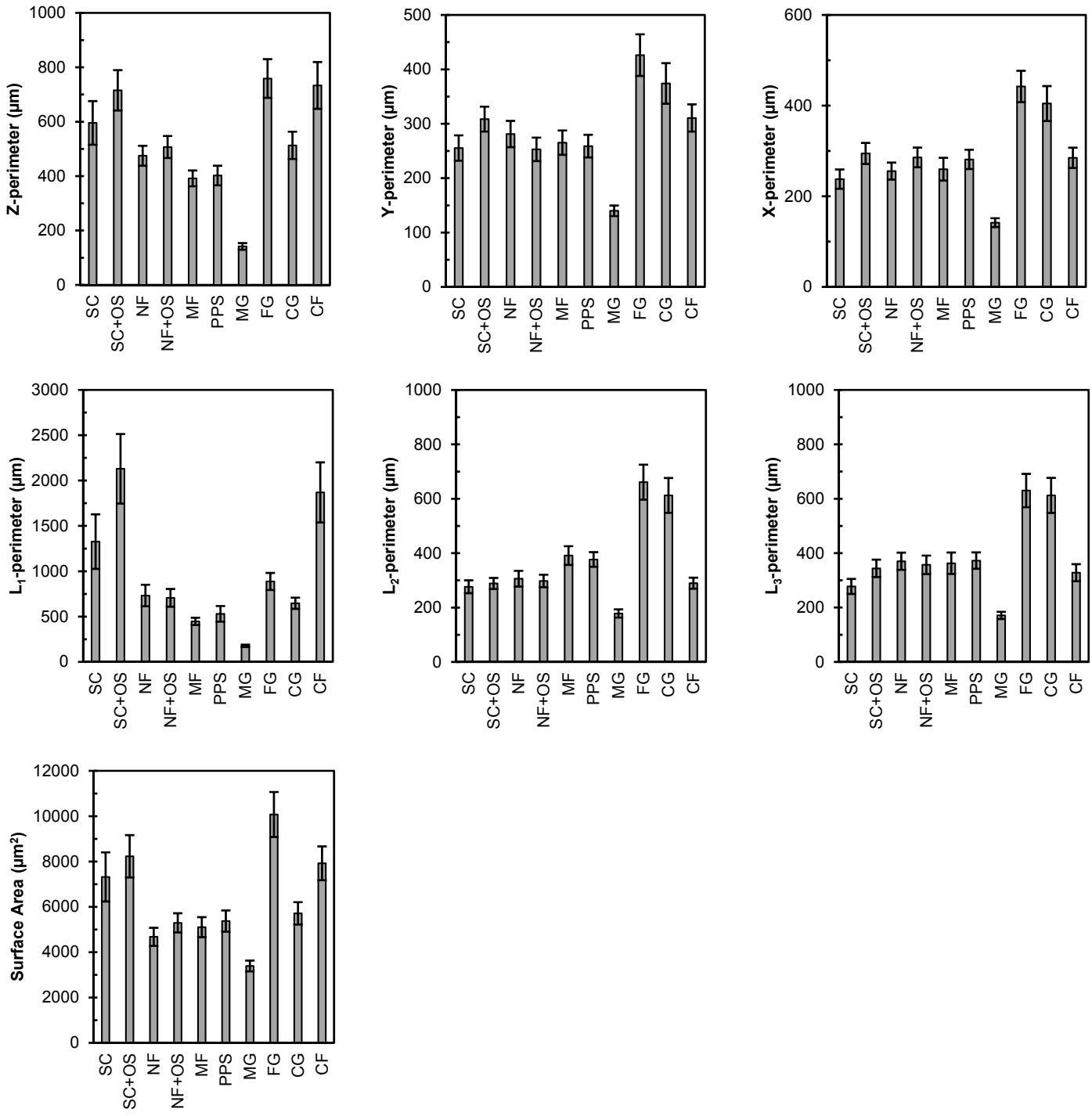

Fig. S2d. Actin shape metric plots. Approximately 100 cells were imaged for each scaffold (see Table 1) and error bars represent 2 standard deviations of the mean. Statistical analysis is in Fig. S3.

Nucleus

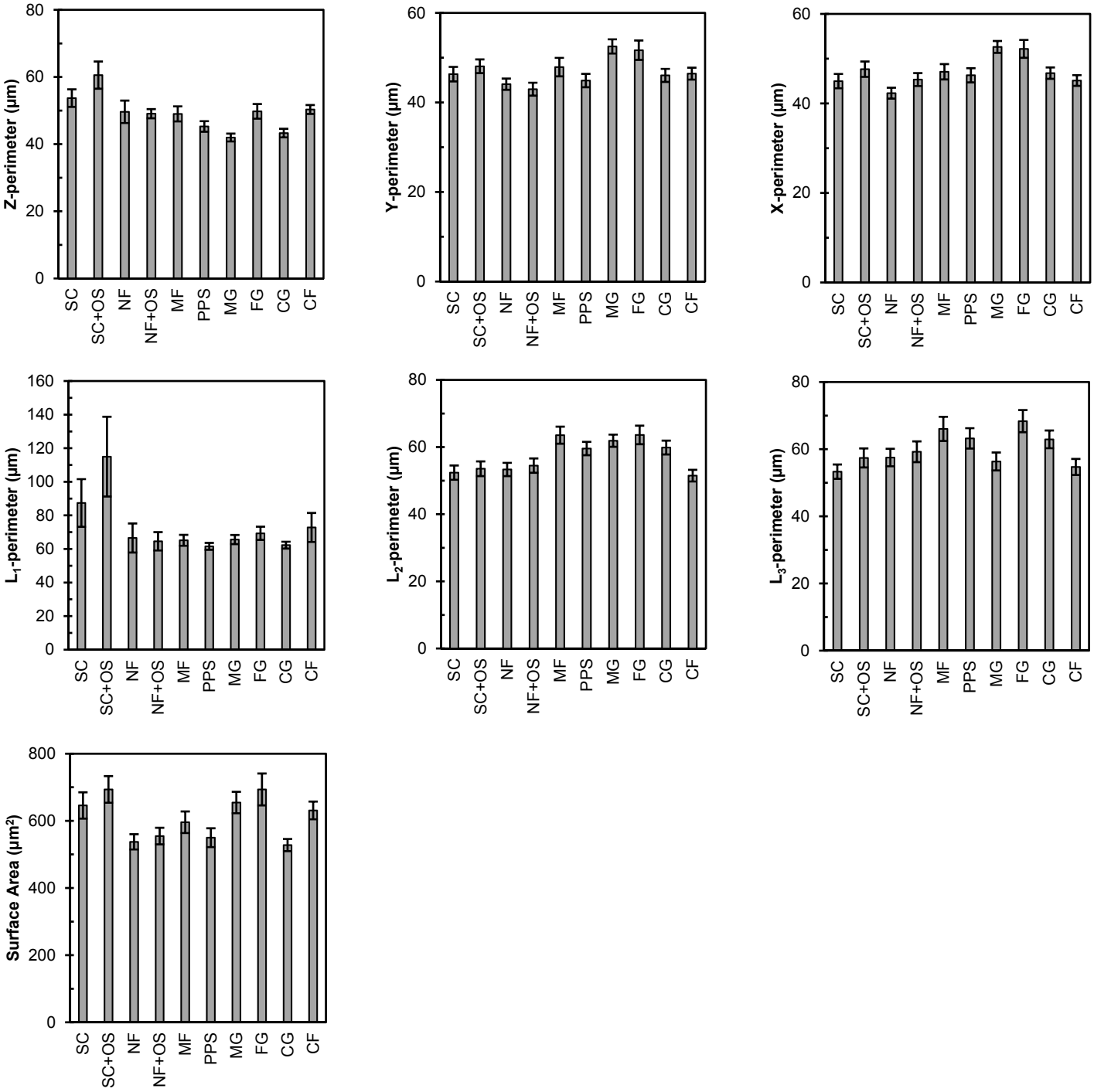

Fig. S2e. Nucleus shape metric plots. Approximately 100 cells were imaged for each scaffold (see Table 1) and error bars represent 2 standard deviations of the mean. Statistical analysis is in Fig. S3.

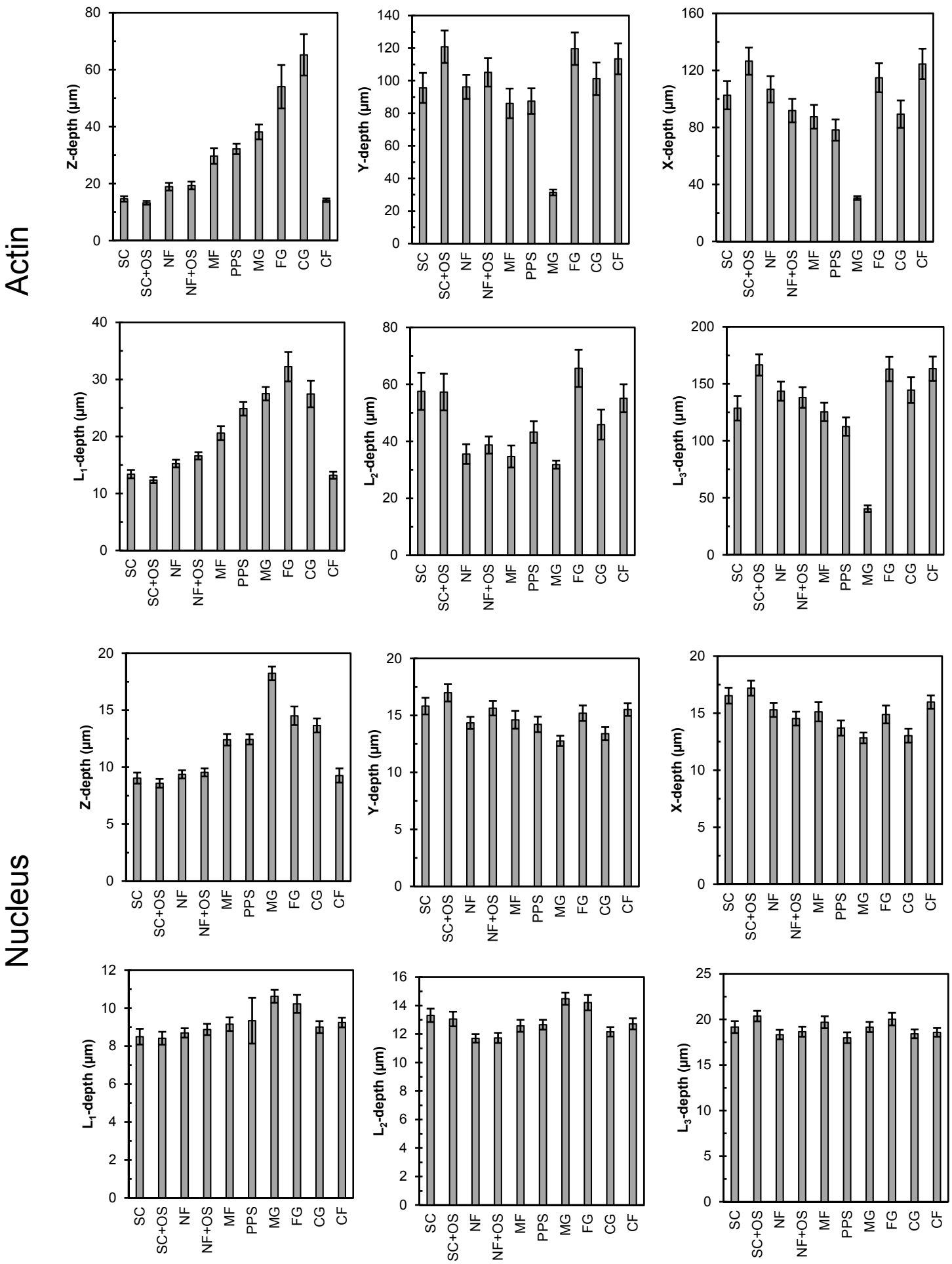

Fig. S2f. Shape metric plots. Approximately 100 cells were imaged for each scaffold (see Table 1) and error bars represent 2 standard deviations of the mean. Statistical analysis is in Fig. S3.

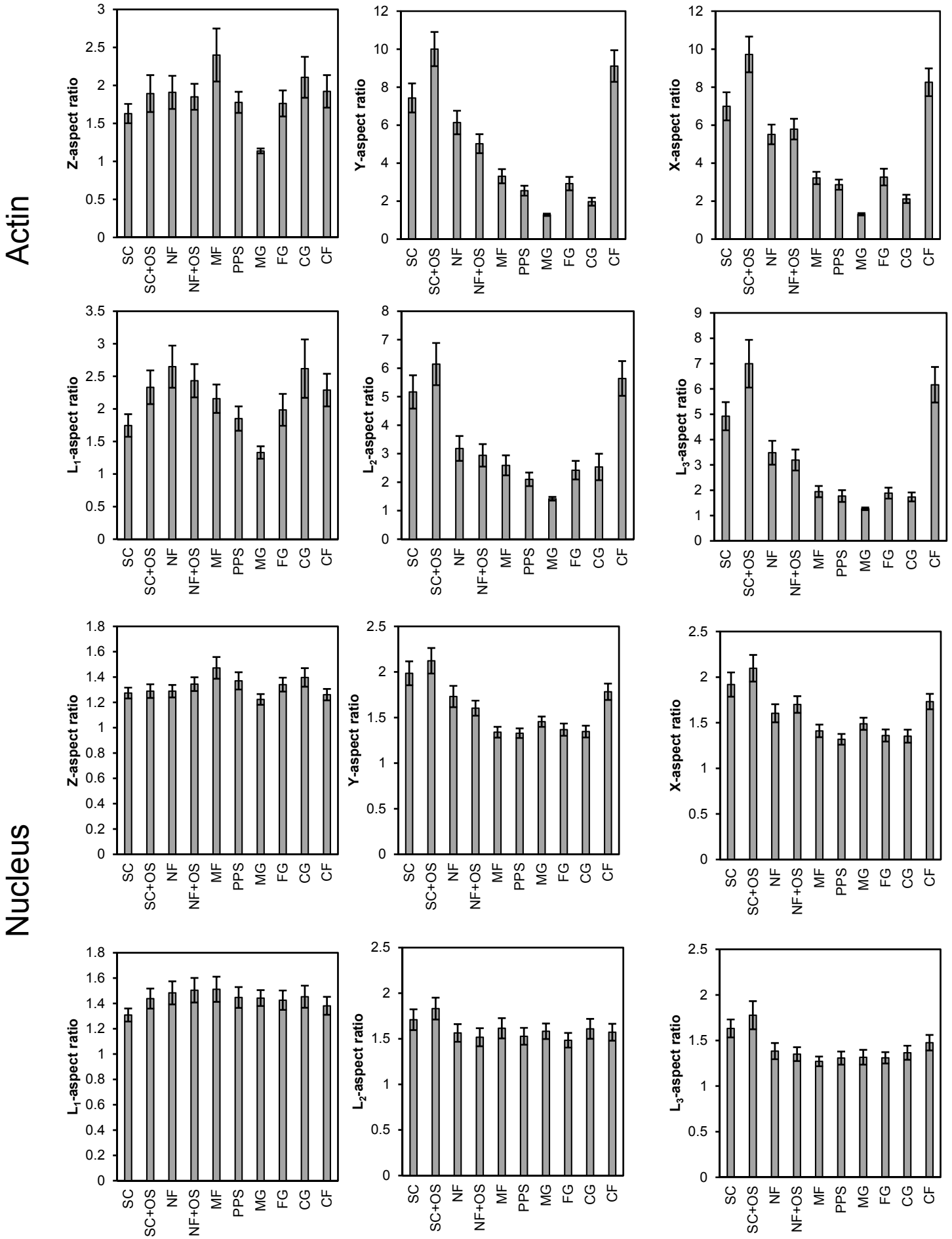

Fig. S2g. Shape metric plots. Approximately 100 cells were imaged for each scaffold (see Table 1) and error bars represent 2 standard deviations of the mean. Statistical analysis is in Fig. S3.

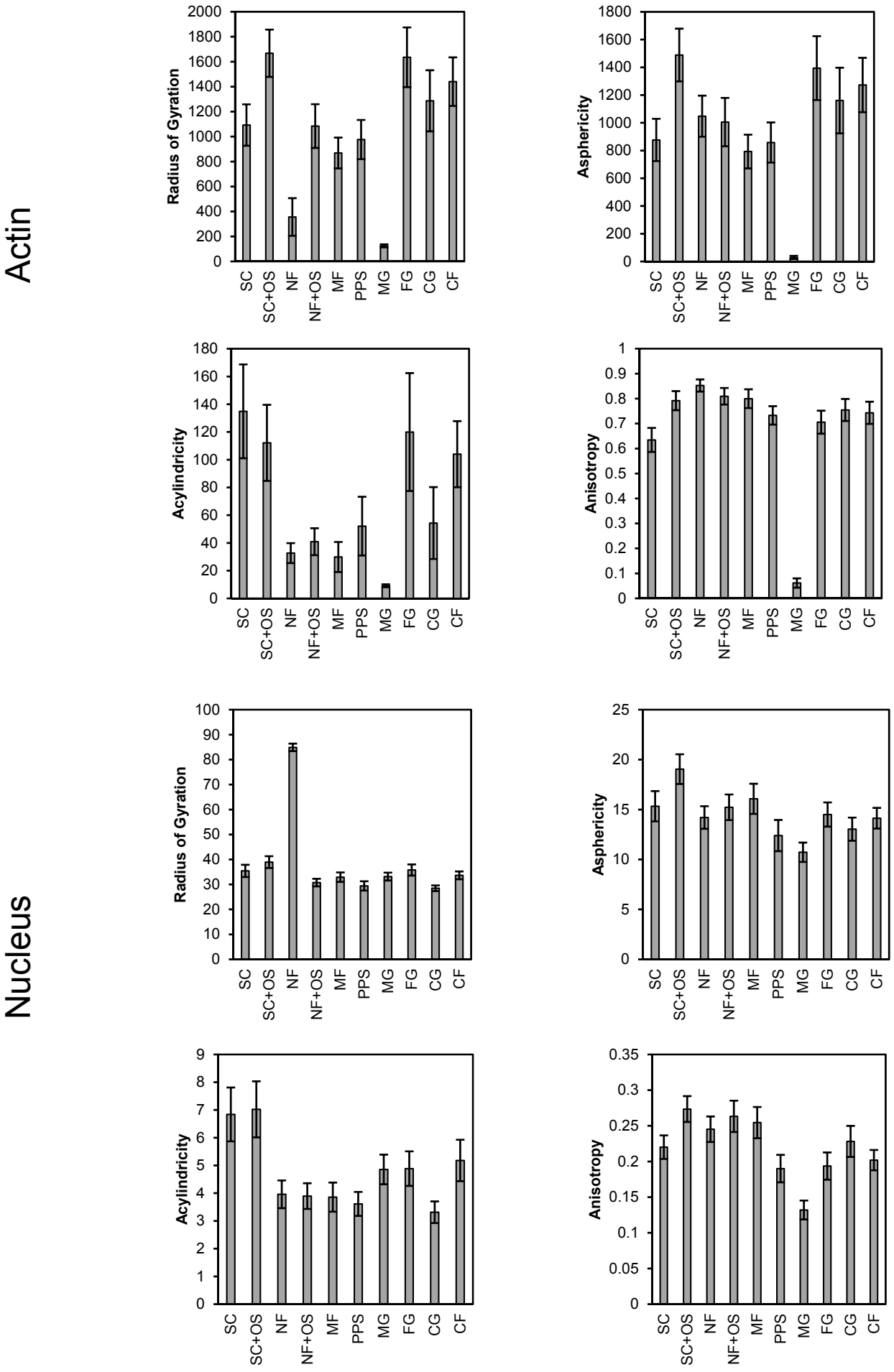

Fig. S2h. Shape metric plots. Approximately 100 cells were imaged for each scaffold (see Table 1) and error bars represent 2 standard deviations of the mean. Statistical analysis is in Fig. S3.

(a) Actin

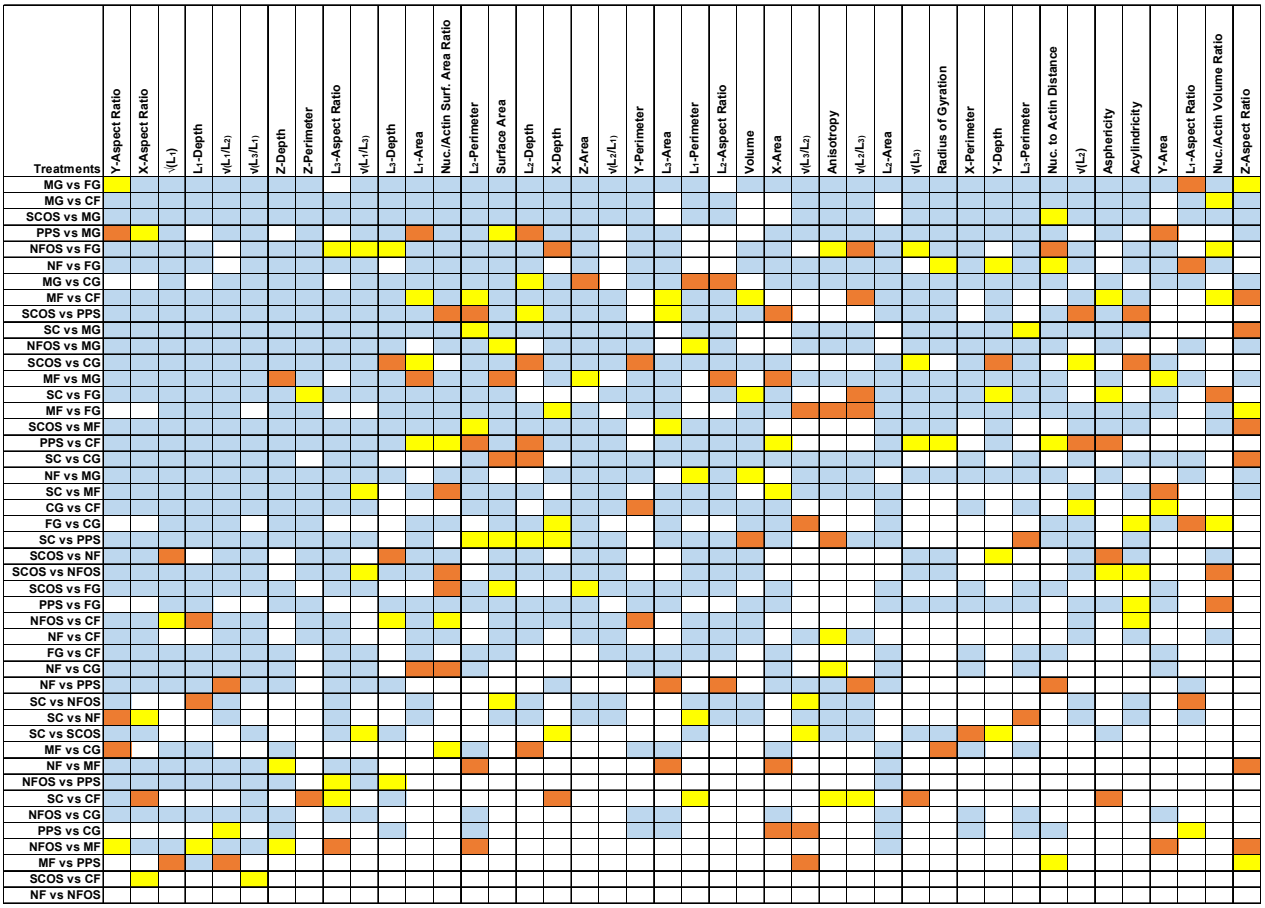

(b) Nucleus

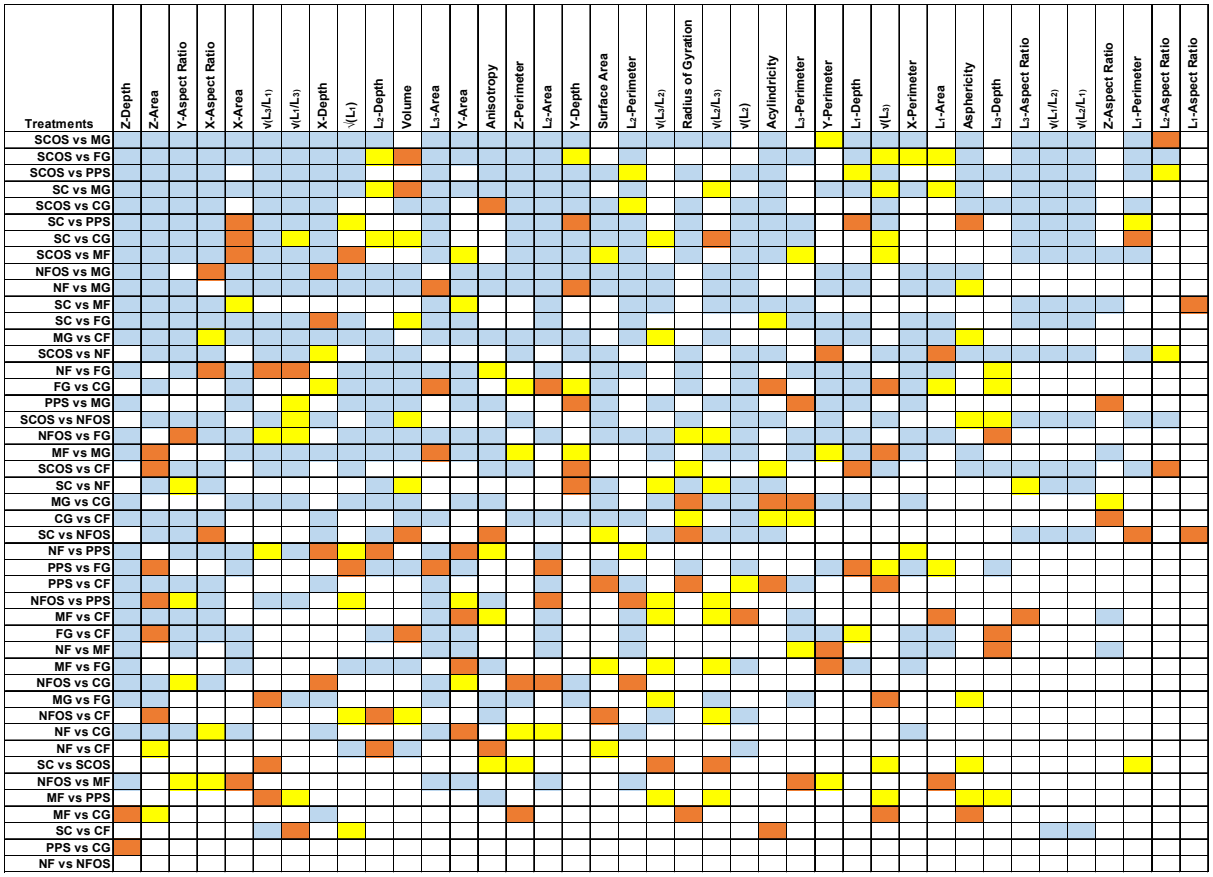

Fig. S3. Statistically significant differences. Comparison of scaffold groups with Tukey's HSD test for multiple comparisons following a one-way ANOVA. The orange boxes indicate a p-value of < 0.05, yellow boxes indicate a p-value of < 0.01, and blue boxes indicate a p-value of < 0.001. The shape metrics and group pairings are sorted from lowest to highest by the sum of the p-values for the columns and rows, respectively. Therefore, the columns towards the left and rows near the top have more significant differences (shaded boxes).

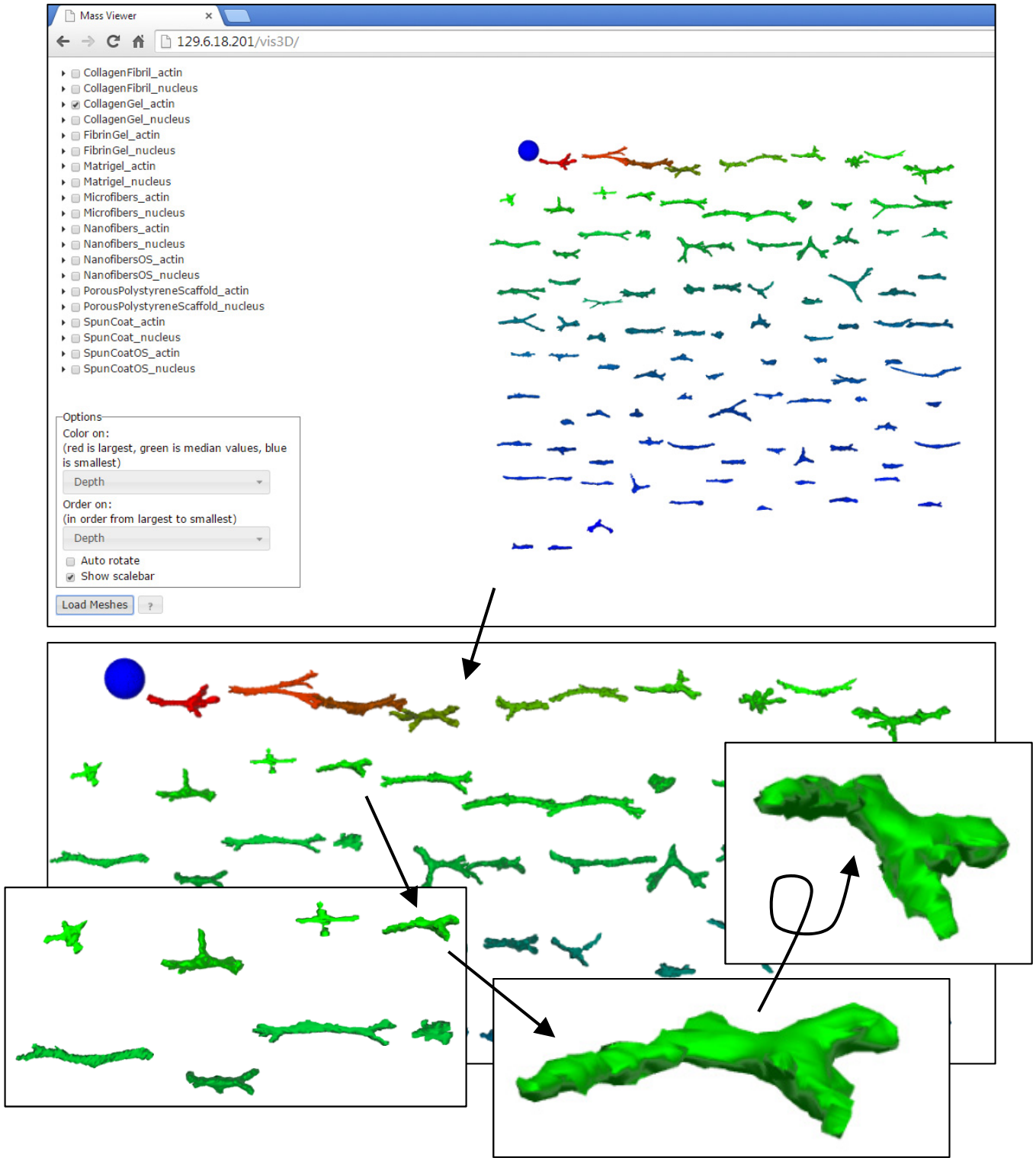

Fig. S4. All data collected in the current work has been deployed online for public access: https://isg.nist.gov/deepzoomweb/stemcells3d/index.html. An interactive 3D-cell viewer has been built to enable online browsing of the data. The cell viewer enables rapid visualization of cells in 3D, with the ability to view the entire dataset, entire scaffold groups, or custom selections. Individual cells can be selected to examine at higher resolution, with the ability to freely rotate the cell. Cells displayed in the 3D-viewer are always aligned according to their gyration tensor moments. When cells first appear on-screen after clicking "Load Meshes": the L_1-axis projects into the computer screen, the L_2-axis runs top to bottom on the computer screen and the L_3-axis runs left to right along the computer screen. The cell viewer enables results from quantitative cell shape measurements to be verified via visual examination of cell shapes. Cells can be sorted and colored according to shape metrics. Results shown are for Collagen Gel, sorted and colored by Z-depth (L_1-axis projects into the computer screen).

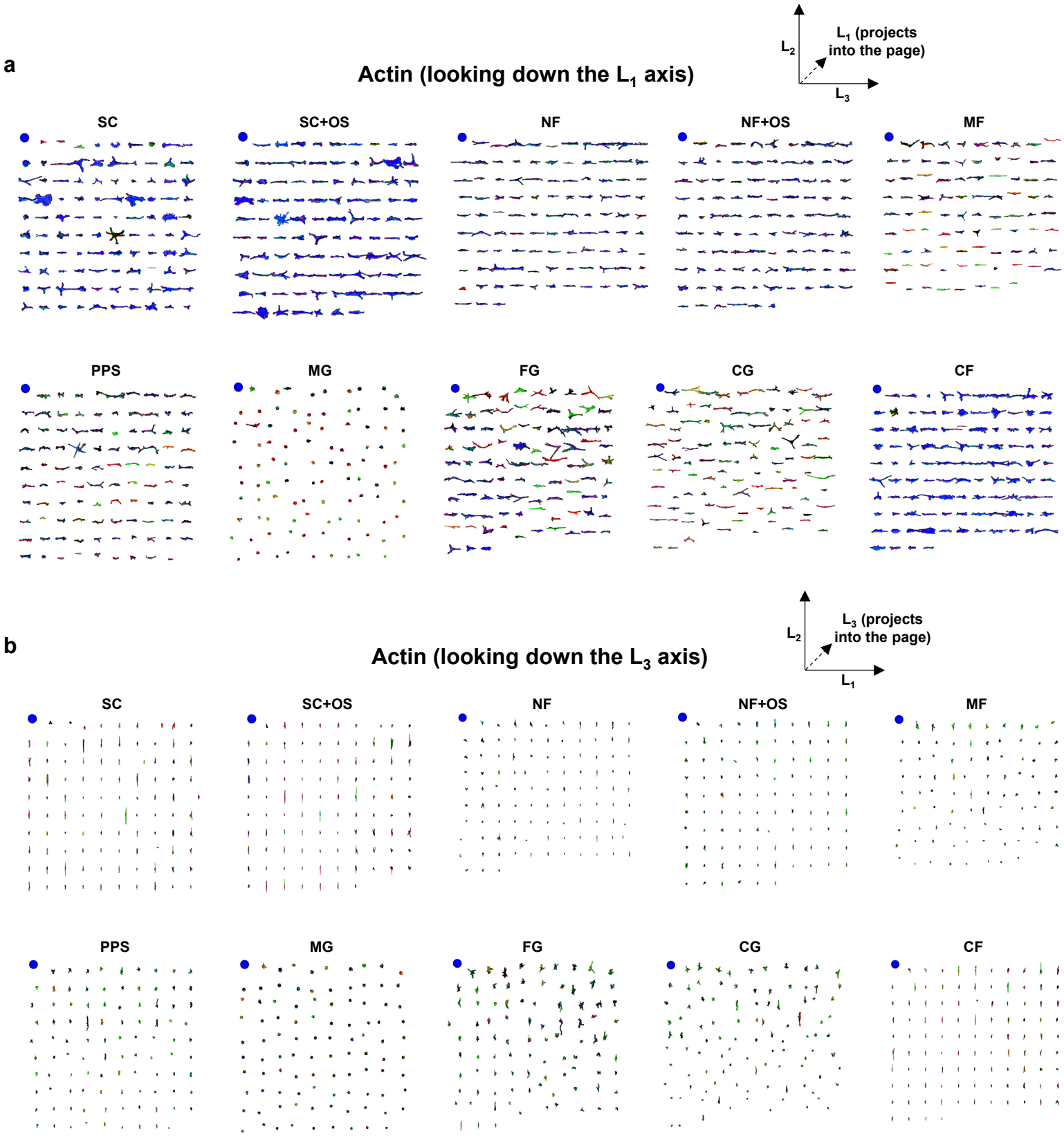

Fig. S5a,b (a) A display of actin in all cells analyzed in the current work was assembled from screen captures of the 3D cell viewer. Ten groups of cells are shown that correspond to the 10 treatments groups explored in the current work. Within each cell group, the individual cells are ordered by L_1-depth with the largest L_1-depth at the upper left of each treatment group. The blue spheres at the upper left of each scaffold group are 100 μm in diameter and serve as the size scale. A guide to the gyration tensor axis alignments is given at the top of the panel. (b) Same as (a) except cells have been rotated 90° on their L_2-axis, so that L_1-depth can be compared amongst treatments.

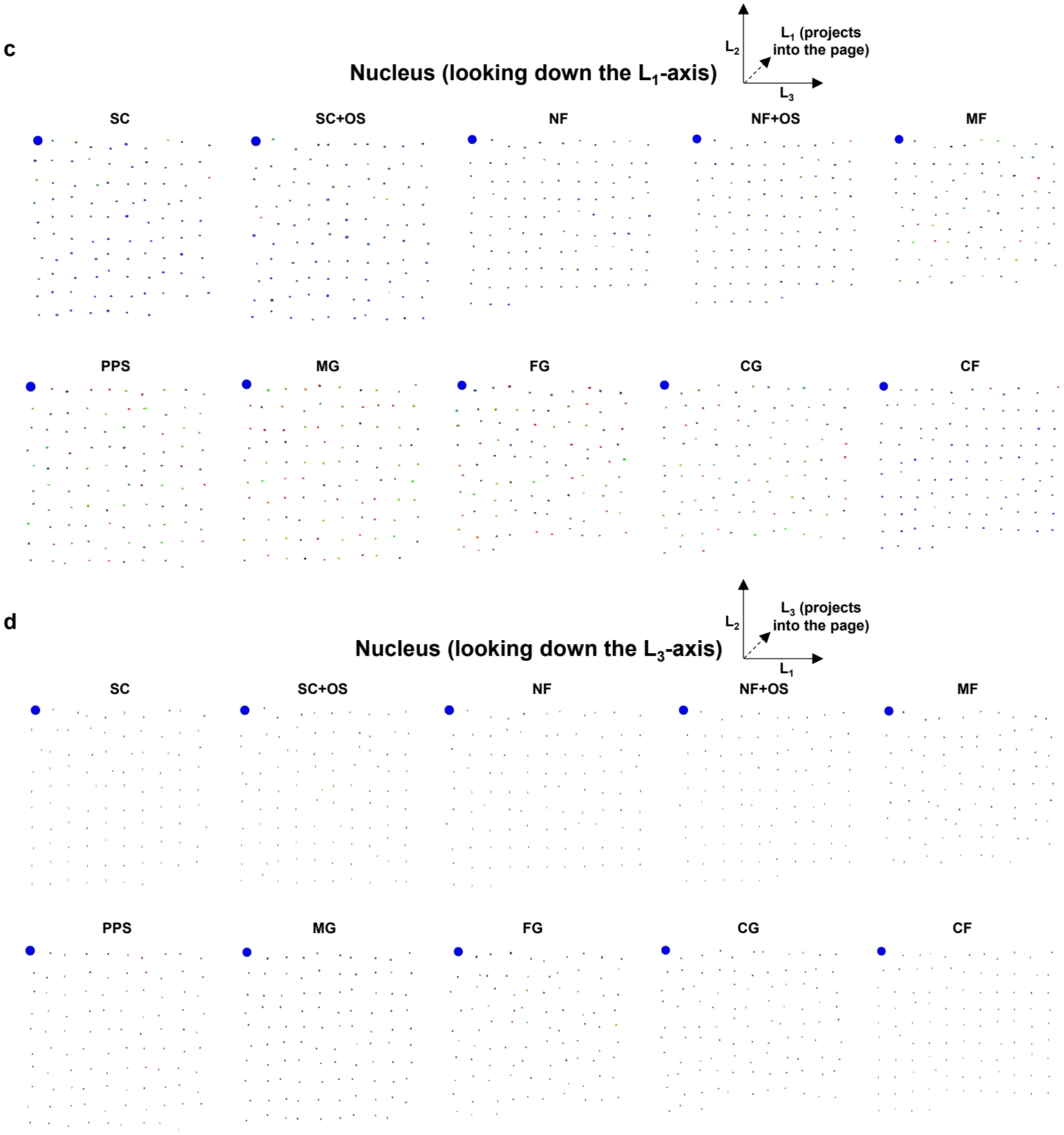

Fig. S5c,d. (c) A display of nucleus in all cells analyzed in the current work was assembled from screen captures of the 3D cell viewer. Ten groups of nuclei are shown that correspond to the 10 treatments explored in the current work. Within each cell group, the individual nuclei are ordered by L_1-depth (largest L_1-depth is in the upper left of each scaffold group). The blue spheres in the upper left of each scaffold group are 100 μm in dia. and serve as the size scale. A guide to the gyration tensor axis alignments is given at the top of the panel. (d) Same as panel (c) except nuclei have been rotated 90° on their L_2-axis, so that L_1-depth can be compared amongst treatments.

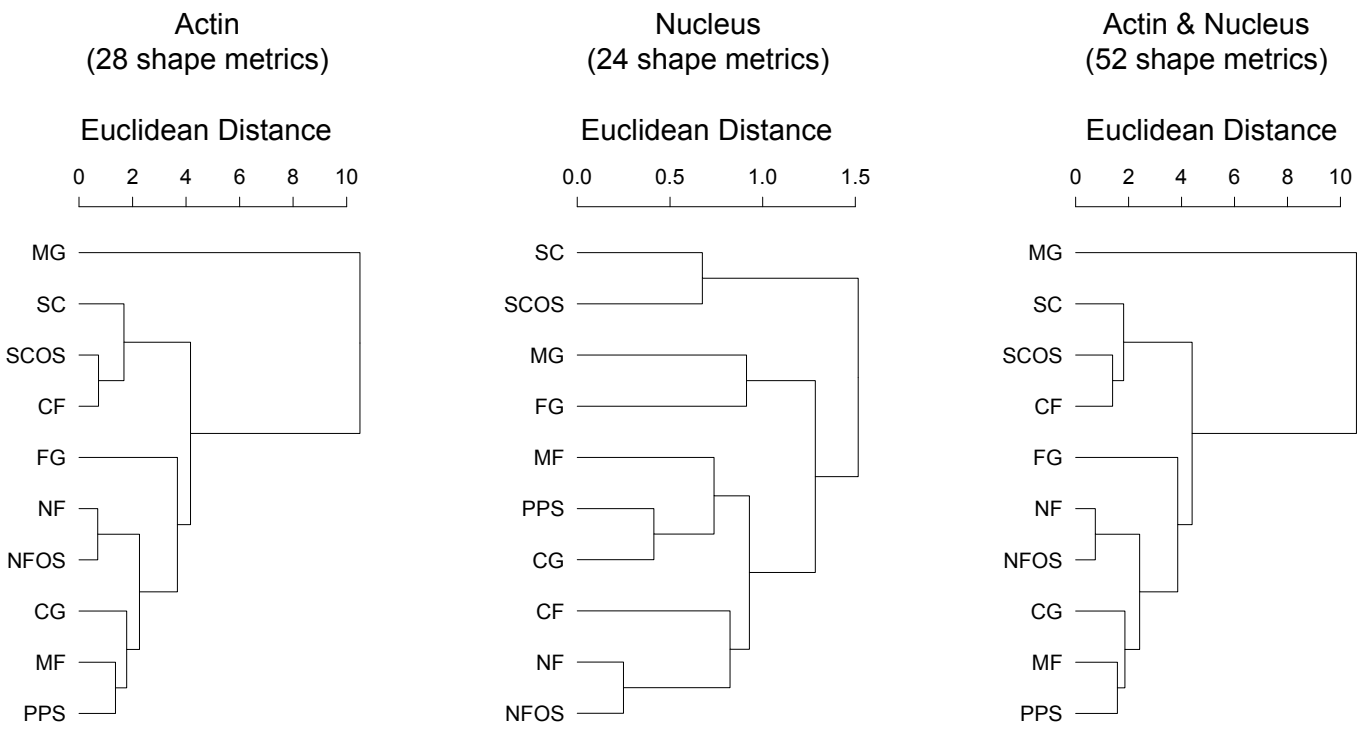

Fig. S6a. Hierarchical cluster analysis of average values for actin, nucleus, and actin & nucleus shape metrics. All of the input data used for clustering was $\log_2$-transformed average (10% trimmed mean) values. The dendrogram for average values for actin shape metrics is from the hierarchical cluster analysis shown in the manuscript (Fig. 4). The scales for the dendrograms are Euclidian distance in multidimensional space. The number of metrics is indicated below the name for each dendrogram and the shape metrics used for clustering were selected from the full list (Fig. S1) by removing metrics calculated from cells that were not oriented by gyration tensor moments.

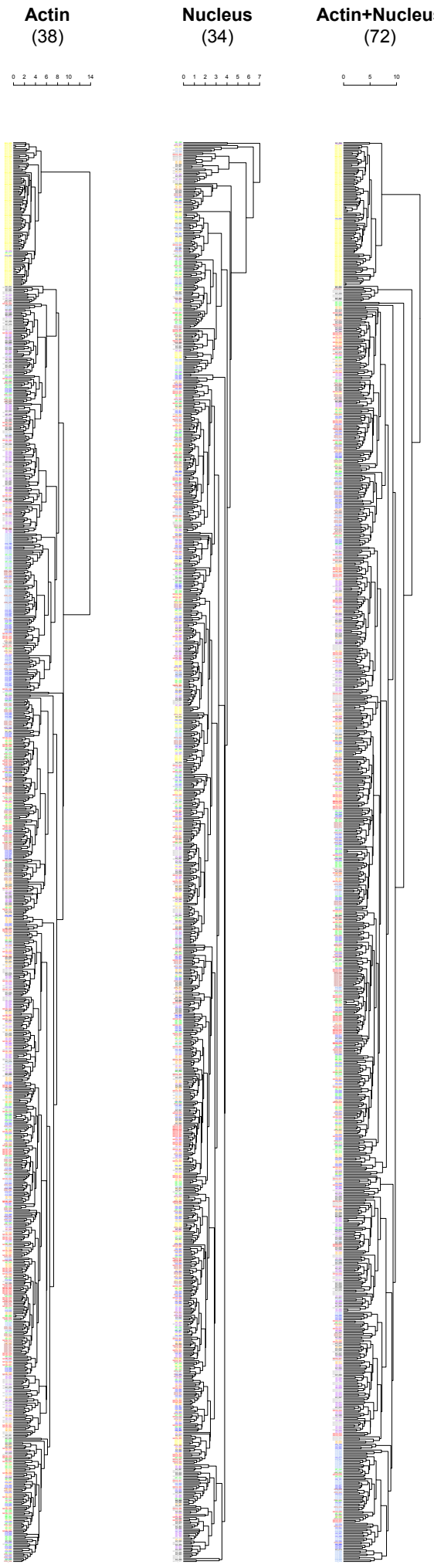

Fig. S6b. Hierarchical cluster analysis of individual cells for actin, nucleus, and actin & nucleus shape metrics. Data were $\log_2$-transformed and median centered prior to clustering. The scales for the dendrograms are Euclidian distance in multidimensional space. The number of metrics are indicated below the name for each dendrogram and the shape metrics used for clustering were selected from the full list (Fig. S1) by removing metrics calculated from cells that were not oriented by gyration tensor moments.

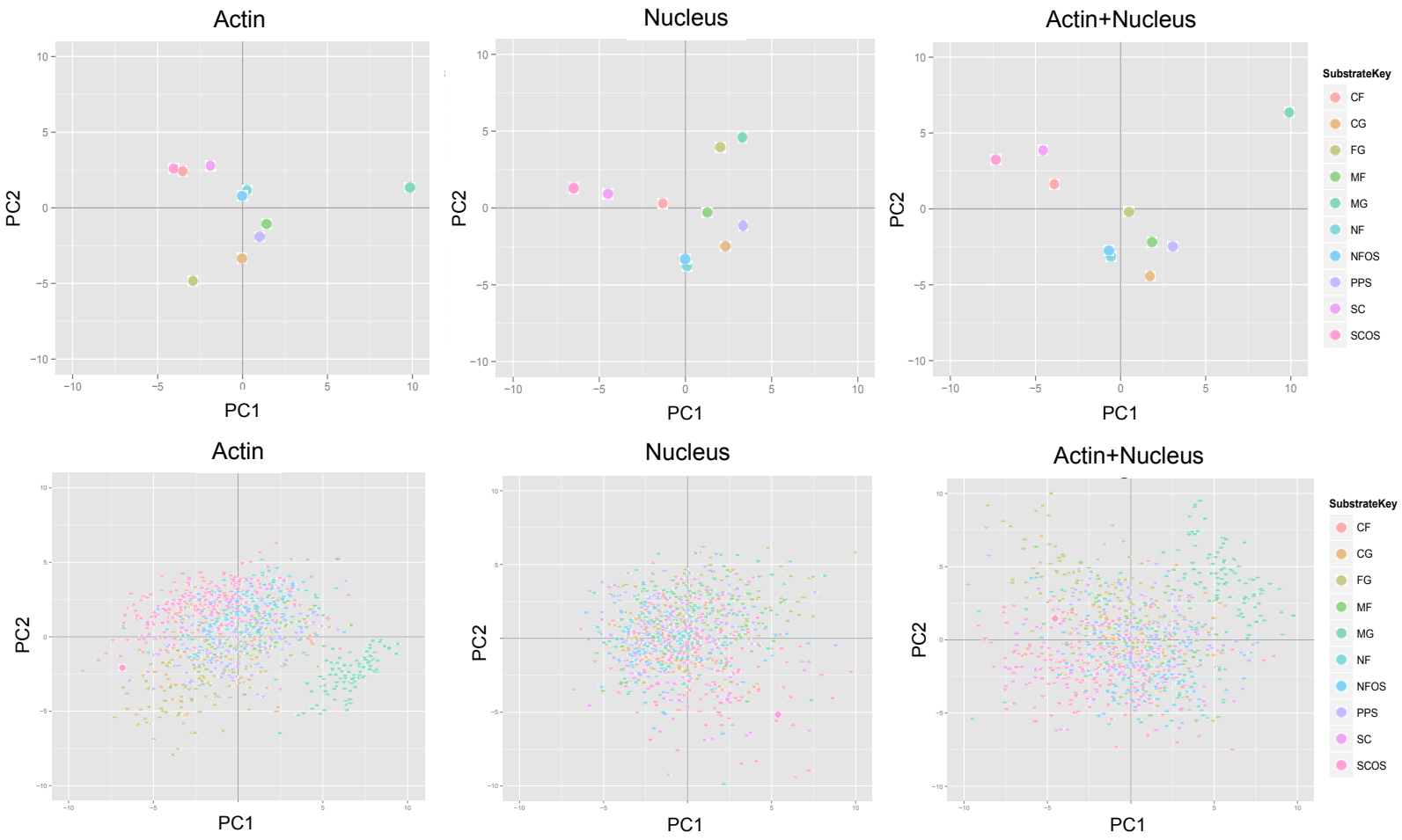

Fig. S7. Principal component analysis (PCA) of cell shape data. Top: PCA analysis of the average values for each treatment group based on the response to the shape metrics included in the HCA for actin (28 shape metrics), nucleus (24 shape metrics), and actin & nucleus (52 shape metrics). Bottom: PCA analysis of individual cells based on the response to the shape metrics included in the HCA for actin (28 shape metrics), nucleus (24 shape metrics), and actin & nucleus (52 shape metrics).

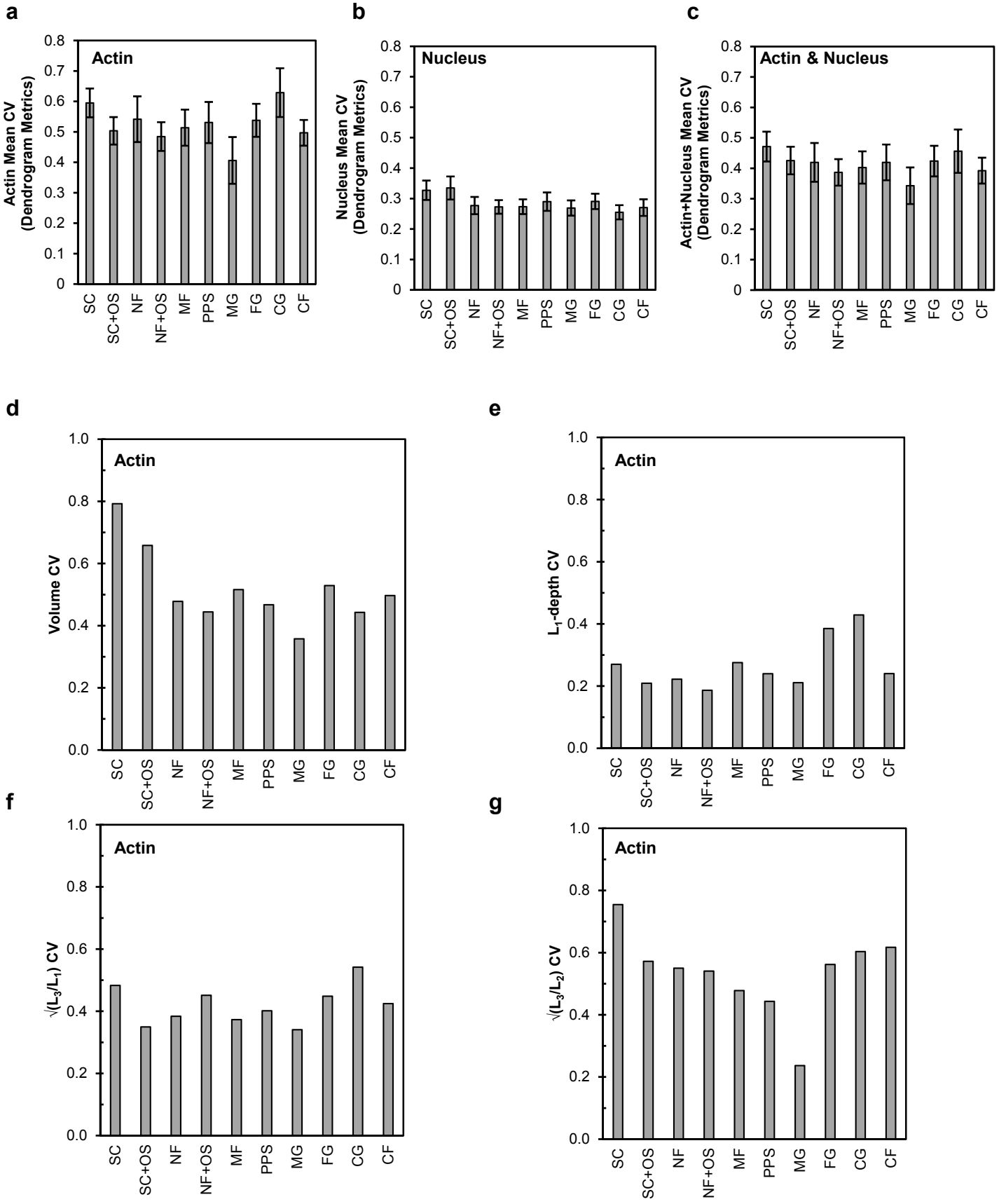

Fig. S8a-g Niche precision. (a) The mean coefficient of variation (CV) analyzed per treatment group for the 28 metrics used for the actin dendrograms (as listed in Fig. S1, n = 28). (b) The mean CVs analyzed per treatment group for the 24 metrics used for the nucleus dendrograms (as listed in Fig. S1, n = 24). (c) The mean CVs analyzed per treatment group for the 52 metrics used for the actin & nucleus dendrograms (as listed in Fig. S1, n = 52). All error bars represent 2 standard deviations of the mean. (d-g) CV for four selected metrics.

h

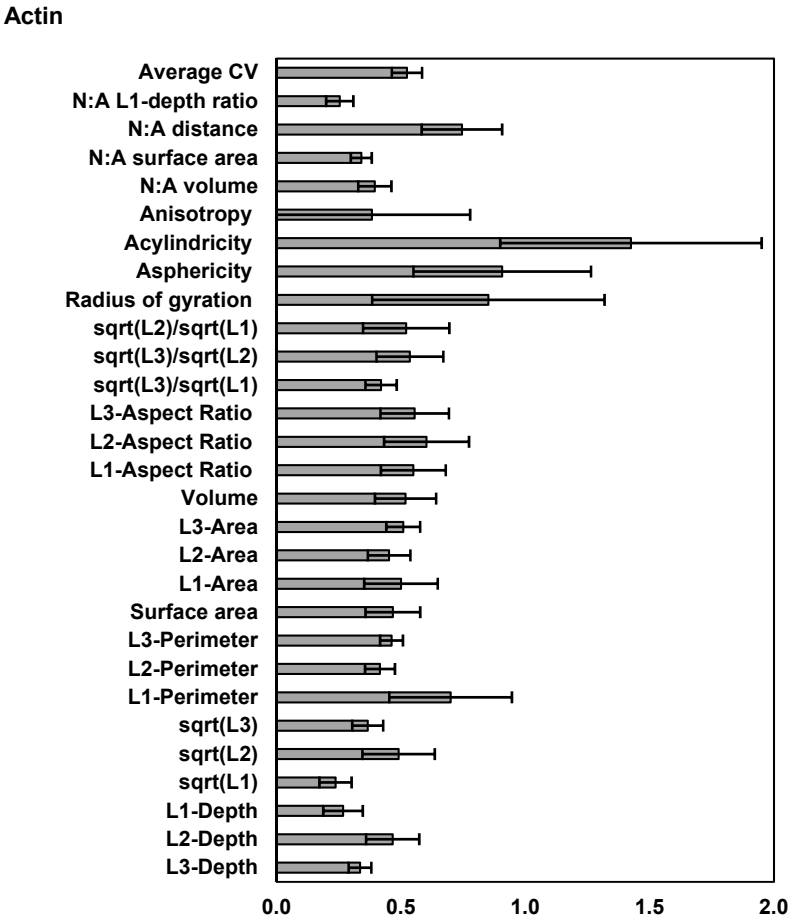

i

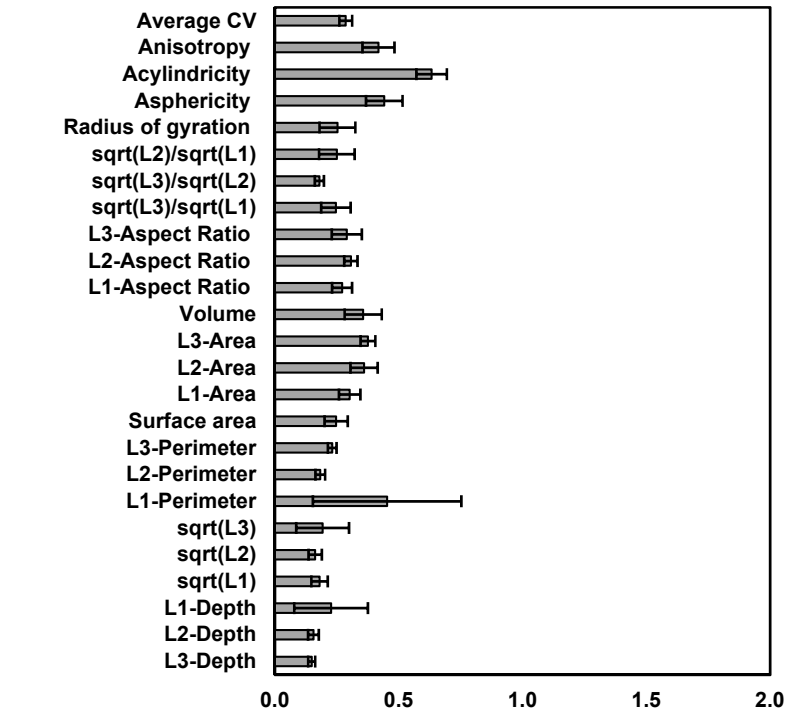

Fig. S8h,i. Shape metric precision. Average CV for each shape metric analyzed in dendrograms, indicating which metrics have the greatest variability among treatment groups. (h) The mean CVs analyzed per treatment for the 28 metrics used for the actin dendrograms (as listed in Fig. S1, n = 10). (i) The mean CVs analyzed per treatment for the 24 metrics used for the nucleus dendrograms (as listed in Fig. S1, n = 10). All error bars represent 2 standard deviations of the mean.

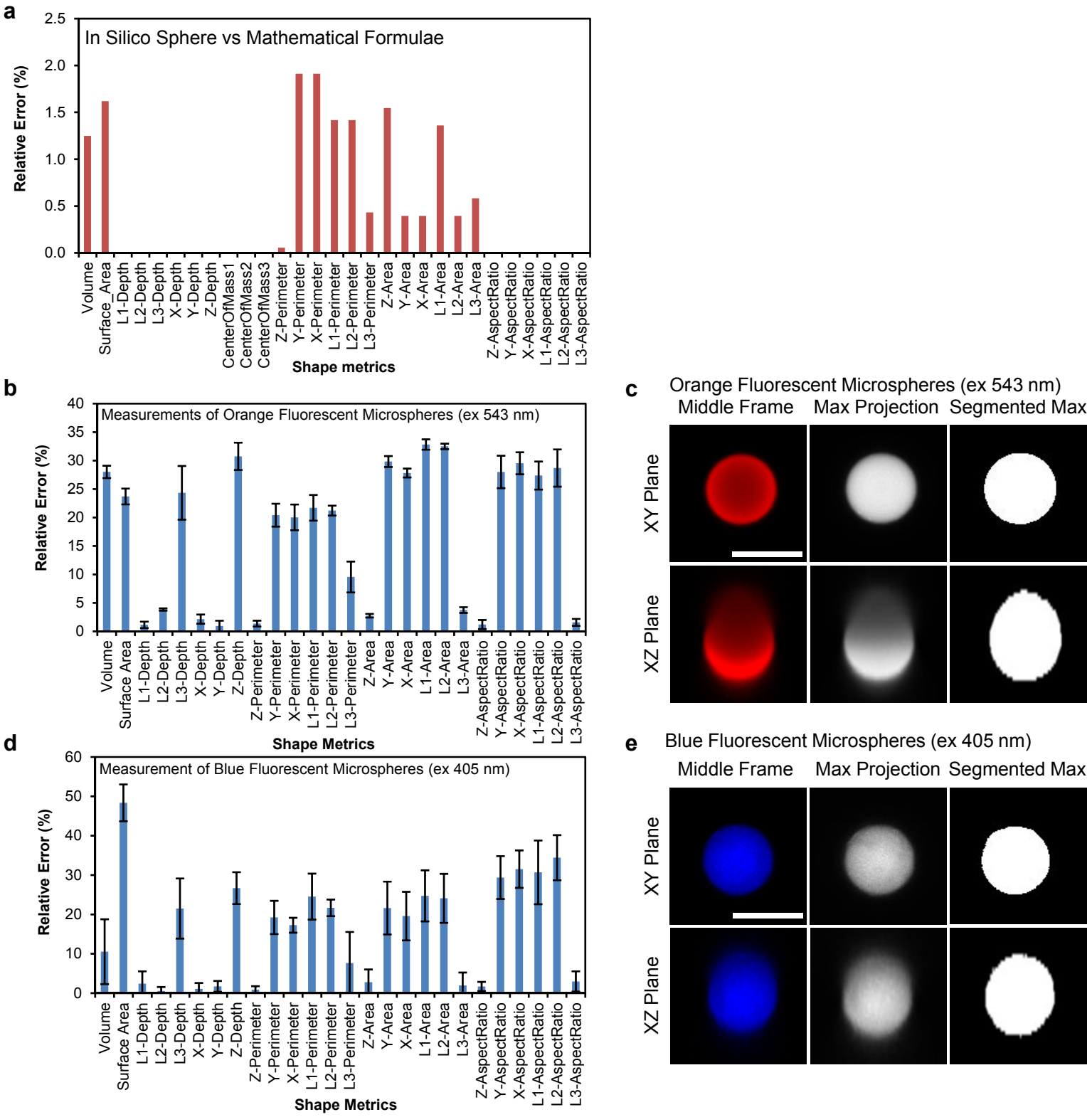

Fig. S9. Relative errors of measured shape metrics. (a) The algorithms used to calculate shape metrics were verified using a synthetic in silico Z-stack of a 3D sphere whose voxel dimensions matched that used for the confocal Z-stack image captures (voxel dimensions of X = 0.240 µm; Y = 0.240 µm, Z = 0.713 µm; sphere dimensions of X-axis dia. = 15.12 µm, Y-axis dia. = 15.12 µm, Z-axis dia. = 14.97 µm). The metric values computed for the in silico sphere were compared with ideal values computed manually for a sphere with 15 µm diameter using mathematical formulae. (b-e) Fluorescent microspheres with known diameter distributions were imaged and analyzed in order to assess the performance of the confocal imaging and image analysis pipeline. Microspheres labeled with fluors corresponding to the 2 channels used for cell imaging were imaged (orange, excitation 543 nm, 14.8 µm dia.; blue, excitation 405 nm, 14.6 µm dia.). Five microspheres were imaged and processed using the same methods as used for cells. Microsphere shape metrics determined from the confocal imaging pipeline were compared with ideal values computed manually for ideal microspheres using mathematical formulae (14.8 µm dia. for actin channel, 14.6 µm dia. for nucleus channel). (b,d) Data are average relative errors and standard deviations (n = 5). (c,e) Example images of microspheres used for the analysis as collected (a single frame from the middle of the stack), after maximum intensity projection, and after processing to yield appropriate segmentations. Scale bars are 15 µm.